Materials Science & Engineering A 769 (2020) 138295

Contents lists available at ScienceDirect

Materials Science & Engineering A

journal homepage: www.elsevier.com/locate/msea

Dislocation structures and the role of grain boundaries in cyclically deformed Ni micropillars

Vahid Samaee[a,*], Stefan Sandfeld[b], Hosni Idrissi[c,a], Jonas Groten[d,1], Thomas Pardoen[c], Ruth Schwaiger[d], Dominique Schryvers[a]

[a] Electron Microscopy for Materials Science (EMAT), Department of Physics, University of Antwerp, Groenenborgerlaan 171, 2020 Antwerpen, Belgium
[b] Micromechanical Materials Modelling (MiMM), Institute of Mechanics and Fluid Dynamics, TU Bergakademie Freiberg (TUBAF), Lampadiusstr. 4, 09596 Freiberg, Germany
[c] Institute of Mechanics, Materials and Civil Engineering, UCLouvain, 1348 Louvain-la-Neuve, Belgium
[d] Institute for Applied Materials (IAM), Karlsruhe Institute of Technology (KIT), Hermann-von-Helmholtz-Platz 1, 76344 Eggenstein-Leopoldshafen, Germany

ARTICLE INFO

Keywords:
Transmission electron microscopy (TEM)
Dislocations
Cell structures
Simulation
Computational analysis

ABSTRACT

Transmission electron microscopy and finite element-based dislocation simulations were combined to study the development of dislocation microstructures after cyclic deformation of single crystal and bicrystal Ni micropillars oriented for multi-slip. A direct correlation between large accumulation of plastic strain and the presence of dislocation cell walls in the single crystal micropillars was observed, while the presence of the grain boundary hampered the formation of wall-like structures in agreement with a smaller accumulated plastic strain. Automated crystallographic orientation and nanostrain mapping using transmission electron microscopy revealed the presence of lattice heterogeneities associated to the cell walls including long range elastic strain fields. By combining the nanostrain mapping with an inverse modelling approach, information about dislocation density, line orientation and Burgers vector direction was derived, which is not accessible otherwise in such dense dislocation structures. Simulations showed that the image forces associated with the grain boundary in this specific bicrystal configuration have only a minor influence on dislocation behavior. Thus, the reduced occurrence of "mature" cell walls in the bicrystal can be attributed to the available volume, which is too small to accommodate cell structures.

1. Introduction

The transition from macro-scale engineering to micro/nano-scale technologies has driven research on mechanical properties of materials towards studying structures with micro- and nanometer dimensions. The determination of the mechanical properties and the understanding of the governing deformation and failure mechanisms of small-scale materials are keys to the design of reliable micro-scale devices. For example, face-centered (fcc) single crystalline micropillars were shown to exhibit much higher yield strength compared to bulk materials typically scaling inversely with the sample size [1,2]. The role of the free surface for the activation of new deformation mechanisms has been recognized, including dislocation starvation [3,4], dislocation- source-limited behavior [5] and source truncation [6–8]. However, depending on the sample size and/or on the initial density of dislocations, plasticity mechanisms of interaction and propagation of dislocations might occur leading to the formation of dislocation patterns [9,10]. On the sub-micrometer scale, low-strain-amplitude cyclic loading can even be exploited to produce dislocation-free samples [11]; the irreversible motion of dislocations leads to unpinning. The dislocations are then pulled to the free surfaces of the crystal by image forces and leave the crystal. Such behavior is quite different compared to cyclic plasticity in bulk fcc metals, which typically exhibit increasing cyclic yield strength because of the generation and arrangement of dislocations, which form specific patterns depending on the crystal orientation and cyclic strain [12]. Also the sample size can affect the dislocation patterns due to cyclic plasticity as shown for thin Cu films [13,14], for which a minimum length scale of ~1 μm was revealed for the specific loading conditions. The traditional view regarding the role of structural interfaces such as grain boundaries is that they constitute obstacles to dislocation motion leading to pile-ups, local stress concentrations and back stresses [15]. Indeed, in the presence of a high angle grain boundary,

* Corresponding author.
E-mail address: Vahid.Samaee@uantwerpen.be (V. Samaee).
[1] Now at: Joanneum Research, Graz, Austria.

https://doi.org/10.1016/j.msea.2019.138295
Received 24 May 2019; Received in revised form 14 August 2019; Accepted 14 August 2019
Available online 20 August 2019

higher strength and higher strain hardening capacity were observed in micrometer-sized Cu [16] and Al [17] bicrystal pillars. The increase of the yield strength with decreasing bicrystal diameter [18,19] was attributed to the higher stresses needed for slip transmission for smaller material volumes. The dislocation reactions that operate at a particular grain boundary affect both the strength and the deformation behavior [20]. When interfaces act as obstacles, higher strength and hardening can be obtained, while significant changes are not expected when the interface acts as a sink for or is transparent to dislocations.

The core question addressed in this work is to determine to what extent the presence of a grain boundary affects the development of the dislocation cell structure in cyclically deformed small scale crystals. High resolution analysis of the dislocation microstructures was conducted using conventional and advanced transmission electron microscopy methods including automated crystallographic orientation mapping in TEM (ACOM-TEM) and nanostrain mapping in TEM. To further elucidate the TEM observations, a computational analysis tailored to the experimental conditions was performed using a finite element based discrete dislocation simulation framework, where dislocations are represented through their eigenstrains [21,22].

2. Materials and methods

A high purity Ni foil (99.999%) (Goodfellow GmbH, Bad Nauheim, Germany) was prepared by mechanical polishing using different diamond suspensions down to 1 µm grain size followed by vibratory polishing with alumina for 3 h (Buehler Vibromet 2). The foil was then annealed at 800 °C in high vacuum for 4 h to obtain grains in the range of 100 µm with a homogeneous crystallographic orientation over the grain areas. Electron Backscatter Diffraction (EBSD) maps were obtained with a Bruker eFlash EBSD detector. Micropillars were fabricated in selected grains and at the grain boundary in-between. The micropillars were fabricated by focused ion beam (FIB) milling using an FEI Scios DualBeam microscope operated at 30 kV acceleration voltage. The pillars had a square cross-section with nominal side lengths of 2 µm, an aspect ratio of approximately 3:1 and almost perpendicular side walls. They were cut from the top while overtilting the sample to compensate for the widening of the beam when penetrating deeper into the sample. The final milling was conducted by single-pass patterning at a beam current of 100 pA. For this study, single crystal pillars with [$\bar{6}$1 10] and [$\bar{6}$ 1 16] normal orientations, referred to as G1 and G2 in the following, and a bicrystal micropillar, i.e. G12, at the grain boundary in-between were prepared. The EBSD map of the local grain structure together with the single and bicrystal micropillars are shown in Fig. 1. Pillars G1 and G2 were both oriented in a multi-slip orientation, while the G12 grain boundary misorientation was ~20°.

Table 1 lists the Euler angles and compression directions parallel to the micropillar vertical axis, and the two slip systems exhibiting the highest resolved shear stresses (RSS). The ratios of RSS of the secondary to the primary slip systems, $\frac{\tau_s}{\tau_p}$, show that the deformation conditions are close to multi-slip in both grains.

Compression-fatigue cycles on different micropillars were performed in order to investigate the effect of the presence of a high angle grain boundary on the formation of dislocation structures during cyclic loading. The pillars were deformed in a scanning electron microscope (SEM) at a loading rate of 150 µN/s to a nominal displacement of 200 nm using a Nanomechanics InSEM 1 nanoindenter equipped with a diamond flat punch of 5 µm diameter. Then, the pillars were unloaded to 15% of the maximum load and reloaded to the same maximum load. After 100 loading cycles, the pillars were fully unloaded. The displacement of the indenter tip was determined from the SEM images recorded during the in-situ experiments to account for uncertainties in the tip displacement measurement of the nanoindenter due to thermal drift.

A FIB-SEM dual beam FEI Helios NanoLab 650 instrument was then used for the preparation of the TEM samples. The micropillars were embedded in an ion beam-assisted Pt protective layer, lifted out, mounted on TEM grids, and milled with a Ga^+ ion beam of 30 kV/0.79 nA and decreasing beam currents finishing with a final polishing step at 2 kV/39 pA to reach a TEM sample thickness of 200–300 nm. In order to investigate the microstructure of the deformed micropillars, two-beam bright-field TEM (BF-TEM) imaging, ACOM-TEM (Nanomegas, Inc.) and nanostrain mapping in TEM (Topspin, Inc.) were used in an FEI Tecnai G2 microscope operating at 200 kV. Precession electron diffraction (PED) was adopted to minimize dynamic effects and to facilitate the automated indexing of the diffraction patterns.

3. Results

3.1. In-situ SEM cyclic deformation

In Fig. 2, the deformed pillars after 100 loading cycles are shown together with the identified slip systems. In all micropillars, slip steps or traces on the surfaces indicate the activation of at least two different slip systems in agreement with the multi-slip condition. The single crystal pillar G1 exhibits large slip steps (Fig. 2a), while the pillar G2 exhibits much smaller ones (Fig. 2b). As evidenced by the pronounced slip steps, pillar G1 accumulated higher plastic strains along the loading direction compared to pillars G2 and G12, i.e. ~15% compared to ~5% and ~7%, respectively, based on the height of the deformed micropillars.

Due to pronounced slip in G1 during the first loading cycle (Fig. 3a), the initial nominal displacement of 200 nm was exceeded significantly resulting in the much larger accumulated strain. The large strain bursts are indicators of a low density of dislocations in the original

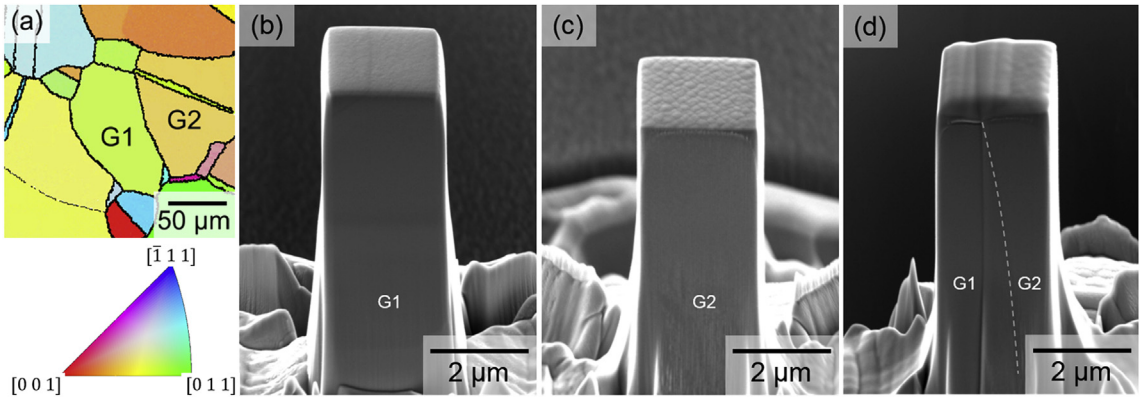

Fig. 1. (a) EBSD map of the high-purity Ni foil after annealing; (b), (c) SEM micrographs (52° tilt angle) of single crystal micropillars, which were fabricated by FIB-milling in selected grains G1 and G2; (d) bicrystal pillar G12 containing the grain boundary in-between grains G1 and G2.

Table 1
Crystallographic orientations of the single crystal pillars and the slip systems with the highest Schmid factors. The ratios of the resolved shear stresses of the respective slip systems indicate multi-slip conditions.

Pillar	Euler angles ϕ_1, φ, ϕ_2	Compression direction	Primary slip system	Schmid factor	Secondary slip system	Schmid factor	$\frac{\tau_s}{\tau_p}$
G1	261°, 33°, 83°	$[\bar{6}\,1\,\bar{10}]$	$(111)[01\bar{1}]$	0.492	$(\bar{1}1\bar{1})[01\bar{1}]$	0.456	0.93
G2	261°, 22°, 101°	$[\bar{6}\,1\,\bar{16}]$	$(111)[01\bar{1}]$	0.497	$(\bar{1}1\bar{1})[01\bar{1}]$	0.481	0.97

microstructure [23]. The single crystal pillar G2 showed smaller strain bursts than G1, while plastic deformation was initiated at a lower stress. While the loading curve of pillar G12 exhibits steps in the first cycle (Fig. 3a), the deformation can be regarded as generally continuous. The different slopes of the elastic portions of the loading curves of G1 and G2 reflect the different Young moduli, i.e. 204 GPa and 168 GPa for G1 and G2, respectively. The reduced slope of the G12 pillar is caused by the thick Pt layer deposited on the top of the pillar (Fig. 1d) which smoothed out the height differences between the two different grains.

The strain increases with increasing number of cycles (Fig. 3b), which is expected for compression-compression cycles and likely enhanced by cyclic creep effects [12,24]. The strain increases at a somewhat higher rate in case of G1, which is likely related to the higher stress amplitude and mean stress of 160 MPa and 190 MPa, respectively. G2 and G12 were deformed at similar but slightly lower stress amplitudes and mean stresses, i.e. 125 MPa and 140 MPa in the case of G2, and 125 MPa and 150 MPa for G12.

3.2. Post-mortem TEM analyses

TEM investigation of the pristine Ni bulk sample revealed that only few dislocations were initially present within the grains and near the grain boundary (not shown). After cyclic deformation a network of dislocations and dense dislocation tangles were observed as shown in Fig. 4a and b. Such dislocation patterns have also been observed in the microstructure of monotonically deformed Ni micropillars [9].

G1 has a somewhat higher average dislocation density than G2, which suggests that G1 has experienced a higher degree of plastic activity. This is consistent with the higher amount of accumulated plastic strain in G1 (compare Fig. 3a). However, a higher dislocation density ρ does not necessarily mean that the amount of accumulated plastic strain γ is higher. For example, after heavy dislocation activity all dislocations might have left the sample through the surfaces resulting in zero density but significant amount of plastic strain. In terms of the morphology of the dislocation structure, three different regions, which were subjected to very different boundary conditions and therefore experienced very different stress states [25], can be distinguished. The top of the pillar is mechanically constrained due to the friction acting between the flat punch indenter and the surface. This creates stress concentrations triggering dislocation nucleation, while the constraint may make it more difficult for dislocations to form surface steps and leave the volume through the top surface of the pillar. Therefore, specifically in G2, the dislocation density is higher close to the top surface similar to what other authors have observed [26]. The low stress level in the bulk material underneath the pillar prevents the glide of dislocations out of the pillar, which leads to the dislocation pile-ups in these regions and the shutdown of the sources [27]. In the central part, both pillars exhibit heterogeneous dislocation structures consisting of well-defined wall-like structures (white arrows in Fig. 4a and b) separated by regions of much lower densities. Due to the loading direction and crystallographic orientation of the grains, these structures are early stage dislocation cell structures rather than persistent slip bands (PSB) (cf. [12,28]). Furthermore, the slip systems with the highest Schmid factors (see Table 1) are not coplanar, which increases the probability for dislocation reactions supporting the formation of cell structures. We estimate the distance between the cell walls as 500–600 nm.

A systematic contrast analysis of selected dislocations confined between the veins (Fig. 4c and d) confirms that the majority of them are located on slip systems with high resolved shear stress and exhibit a predominant screw component. The dense wall-like structures consist of randomly oriented dislocations, while a detailed analysis as conducted for the channel dislocations has not been possible. However, the channel region exhibits a pronounced contrast change (Fig. 4c), which was further investigated using automated quantitative orientation and strain mapping combined with a computational analysis of the dislocation microstructure (section 3.3). In monotonically deformed small-scale samples dislocations patterns have been observed [9,10]. Thus, using advanced TEM techniques and computational analyses to characterize the dislocation patterns might also shed new light on the elementary mechanisms controlling the formation of such patterns in monotonically deformed samples.

In contrast to the single crystal pillars G1 and G2, the bicrystal pillar G12 does not exhibit wall-like structures (Fig. 5) but rather early-stage vein structures. The lower dislocation density in G12 compared to G1 is accompanied by a smaller amount of accumulated plastic strain (Fig. 3a). The presence of the grain boundary apparently hinders the formation of veins or wall-like structures. The grain boundary not only acts as an obstacle to dislocation motion, but also affects the resulting stress field of the dislocations through image forces resulting from the elastic mismatch between the two grains. This mismatch may accelerate the transmission or absorption of dislocations [29]).

The wall-like dislocation structures shown in Fig. 4 were visible in

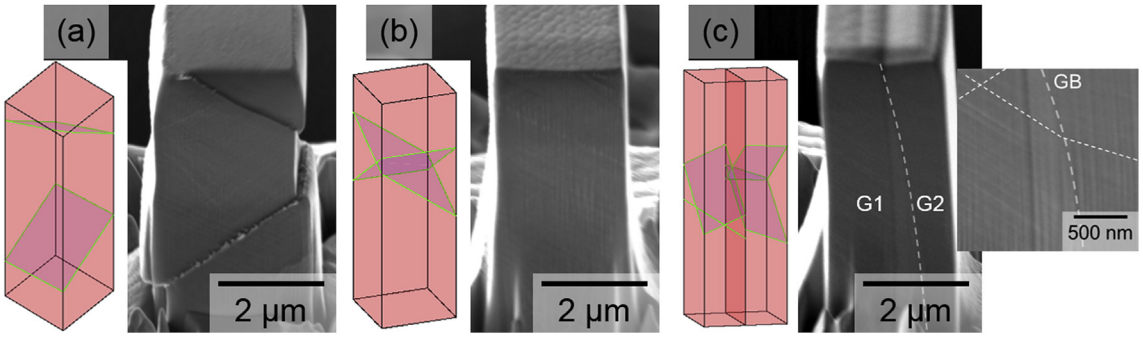

Fig. 2. SEM micrographs (45° tilt angle) of deformed micropillars (a) G1, (b) G2, and (c) G12 after 100 loading cycles. The corresponding sketches show the activated slip planes. The outset of (c) shows the slip lines on the pillar face of the two crystal orientations in G12 at higher magnification.

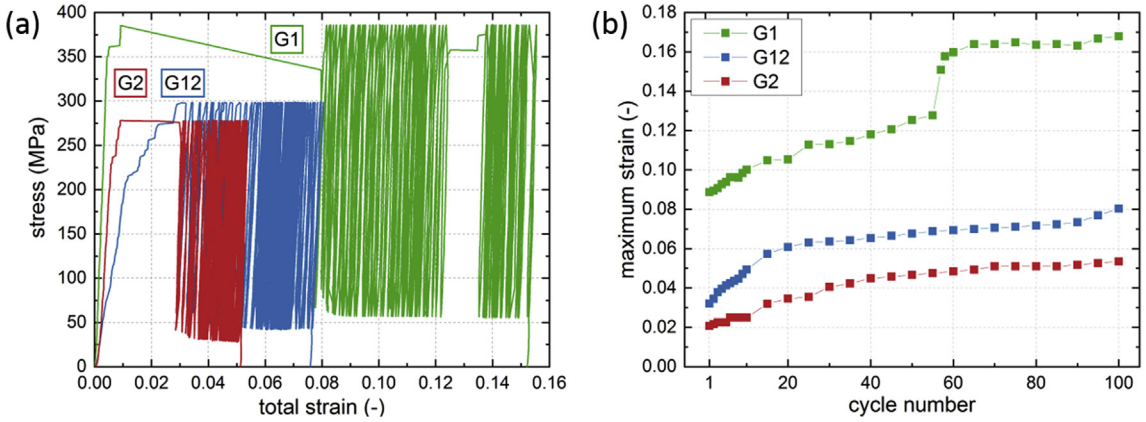

Fig. 3. (a) Stress-strain curves of the three tested pillars G1, G2, and G12. The total strain was quantified based on the analysis of the micrographs recorded during the experiments. The accumulated plastic strain of pillar G1 was ~15% compared to ~5% and ~7% for pillars G2 and G12, respectively. (b) The total strain at the maximum load per loading cycle increased with increasing cycle number and somewhat more pronounced for G1 compared to G2 and G12.

all possible two-beam conditions indicating that different types of dislocations were present. However, the dense character of the wall-like structures and the presence of FIB defects did not allow for quantification and characterization of individual dislocations using diffraction contrast. The local changes of diffraction contrast between the dislocation cell-wall, though, shown in Fig. 4c (lighter region between the two dark regions) and Fig. 4d (darker region between the two walls) can be attributed to local changes of the crystallographic orientation. This implies that the seemingly random structure involves a significant net-Burgers vector, which also excludes the dipole configuration typically found in a PSB wall. To quantify the lattice misorientations, PED [30] and ACOM-TEM [31] were used to generate orientation maps for samples G1 and G12. The electron probe size was ~4 nm and the step size 40 nm with a precession angle of 0.5°. The samples were aligned along the [100] zone axis.

Fig. 6 shows local changes of the crystal orientation close to the top of the G1 micropillar exhibiting dislocation agglomeration. At the position of the dislocation veins, sharp local lattice rotations can be seen caused by excess dislocation density (i.e., geometrically necessary dislocations, GND) that are always accompanied by deformation-induced lattice rotations and long-range internal stresses. This observation also

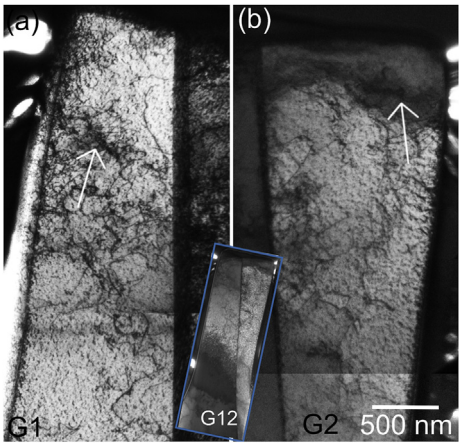

Fig. 5. Bright-field-TEM micrographs of the bicrystalline micropillar G12, with (a) showing G1 and (b) showing G2. The white arrows mark the position of early-stage vein structures in both grains.

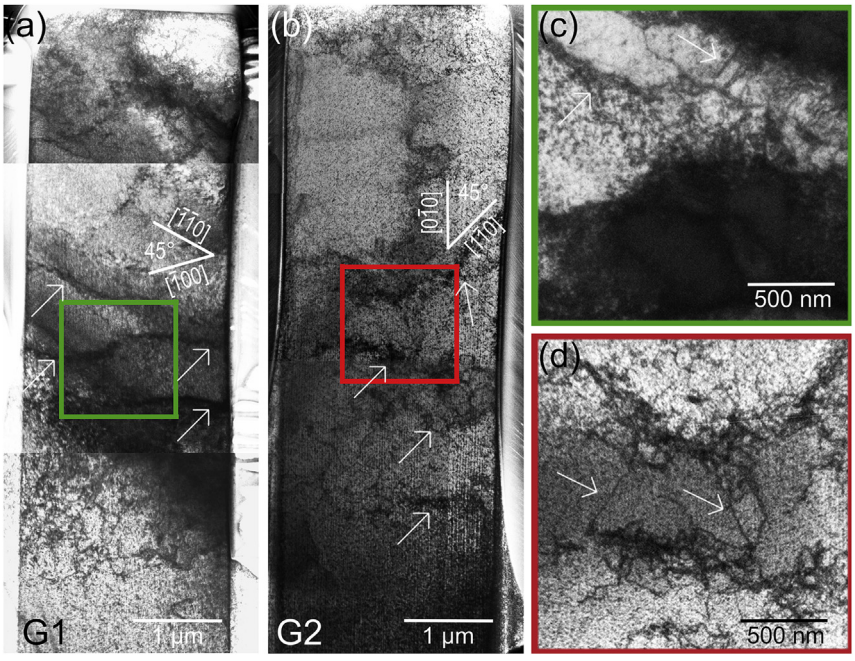

Fig. 4. (a),(b) Bright-field-TEM micrographs of micropillars G1 and G2 after cyclic deformation: The zone axis in both samples is close to [001]. White arrows mark the dislocation cell walls in the structure. (c), (d) Magnified bright-field TEM micrographs of the regions marked in (a) and (b) showing screw dislocations confined between the channels (indicated by white arrows).

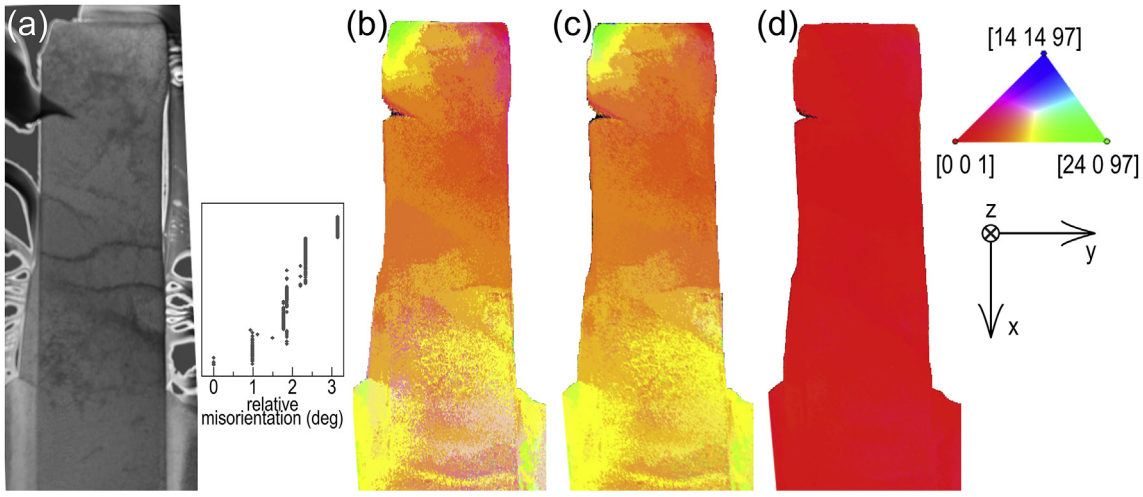

Fig. 6. (a) TEM image of the deformed micropillar G1. The misorientation profile obtained along the dashed white line shows sharp misorientations at the positions of the dislocation cell walls. (b), (c), and (d) the orientation maps of micropillar G1 along X, Y, and Z directions, respectively, taken by ACOM-TEM (to allow for a clear visualization of the misorientations, the inverse pole figure shows a reduced region of the orientation space).

indicates that the dislocation patterns observed after cyclic loading of the micropillars are not PSB-like dislocation dipole configurations but rather dislocation cell walls.

The PED strain maps of micropillar G1 (Fig. 7) reveal pronounced long-range strain fields caused by excess dislocations, which confirm the presence of GNDs. Such cell walls may originate from the interaction of dislocation locks and junctions, which act as obstacles for glissile dislocations such that the local dislocation density increases resulting in even stronger obstacles. Similar to our findings, the presence of internal stress accompanied by enhanced cross-slip was identified in discrete dislocation dynamics simulations studies to be important for the formation of dislocation patterns [23,30–33].

3.3. Analysis of the PED strain fields

The dislocation character and Burgers vector direction were quantitatively analyzed based on the strain fields of the vertical dislocation wall-like structure in order to understand and interpret the strain distributions obtained in the previous section. A very pronounced transverse elastic strain component ε_{xx} can be observed in the middle of Fig. 7 (middle green dashed line).

In order to remove the noise from the strain data, we averaged the strain field along the vertical y direction, because the dislocation bundles are approximately oriented along the vertical direction. During this averaging procedure we apply an additional correction, which takes into account that the bundle indicated by the second green dashed line

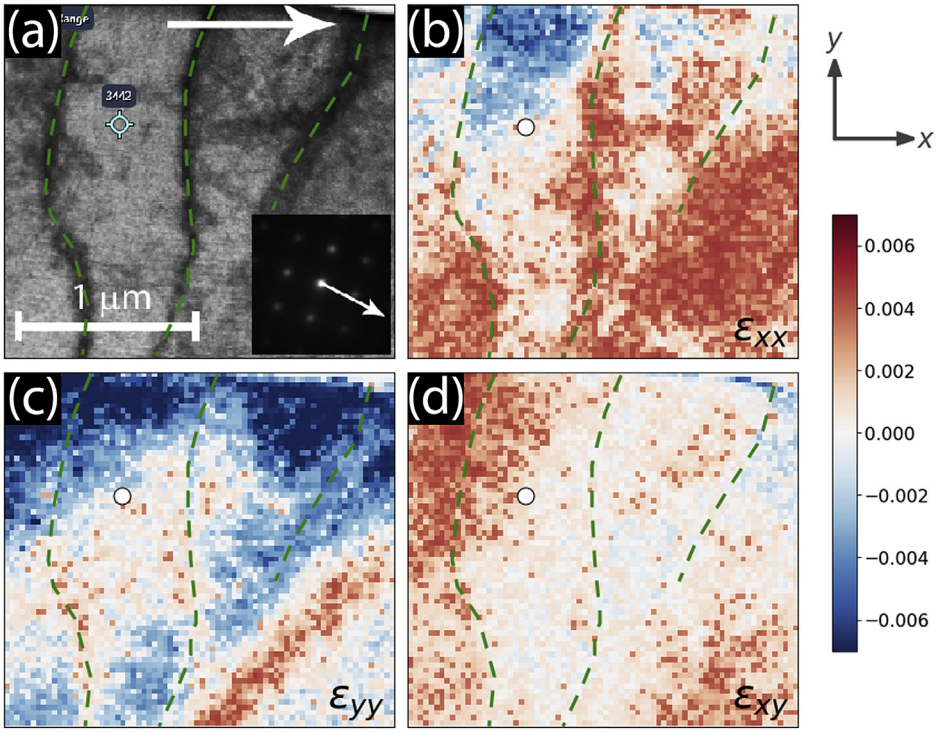

Fig. 7. (a) Virtual bright field TEM image of micropillar G1. The corresponding experimental diffraction pattern is shown in the inset. The white arrows denote the x direction in both spaces. (b), (c) and (d) are the strain fields ε_{xx}, ε_{yy}, and ε_{xy}. The white spot in the maps indicates the position of the reference point in (a), at which the reference diffraction pattern was acquired.

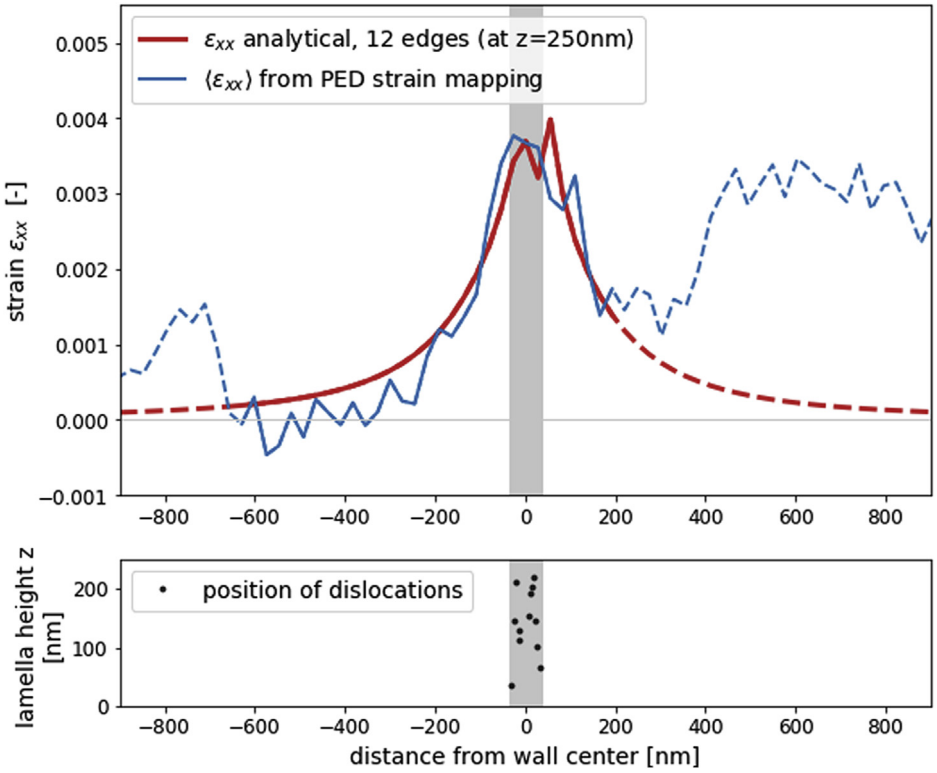

Fig. 8. Analysis of the middle dislocation wall shown in Fig. 7 (green dashed line in the middle). Edge dislocations (black points in the lower graph) were randomly placed inside a narrow region (gray shaded area). Comparing the resulting elastic strain ε_{xx} to the elastic strain obtained experimentally from PED mapping (red and blue curves), best agreement was obtained for 12 edge dislocations. The strain based on PED was obtained by averaging the two-dimensional strain field (Fig. 7b) along the dislocation vein structure. The dashed blue line (upper graph) denotes strains that are mainly caused by the adjacent dislocation veins. (For interpretation of the references to colour in this figure legend, the reader is referred to the Web version of this article.)

is not perfectly straight. Effectively, this correction was done by shifting each row of pixels such that averages are performed over the pixels located at the same distance from the green line. The averaging without this correction also shows that the correction has only a small influence (Detailed data is available in the corresponding *Data in Brief* article). The resulting average normal strain $\langle\varepsilon_{xx}\rangle$ is indicated by the blue curve in Fig. 8.

To identify the dislocation character and Burgers vector direction, we tested all possible combinations of dislocation character and Burgers vector direction and compared them to the shape of the average strains: we placed straight screw or edge dislocations in a thin region corresponding to the dislocation wall thickness (gray shaded region in the lower plot of Fig. 8). For an edge dislocation the Burgers vector could point either into the positive or negative x-direction (see the coordinate system in Fig. 7); for a screw dislocation the Burgers vector has to point towards the positive or negative z-direction (i.e., direction of the lamella height). Then, we computed for all possible combinations of Burgers vector and dislocation character the resulting strain tensor field assuming plane strain conditions. When analyzing the strain distributions for all possible combinations, almost all of them could be directly excluded since the strain would exhibit a change of sign in the wall structure. The only possible combination where the shape of the strain qualitatively matches that of the experimental PED data, is obtained for an edge dislocation with Burgers vector pointing into the negative x-direction. Finally, the number of dislocations as well as their approximate positions were determined by solving an optimization problem with the objective to match the strain distribution shown as solid blue line in Fig. 8 to the experimental data. The best match is obtained for a random distribution of 12 edge dislocations. Their exact positions, however, cannot be uniquely identified since different configurations may yield similar distributions. A typical configuration is shown in the lower graph of Fig. 8, while the red line in the upper graph shows the corresponding strain distribution at the surface of the lamella. Knowing the number of dislocations, we can now compute the excess density in the wall-like structures as $\rho^{GND} \approx 7{\cdot}10^{14}\mathrm{m/m^3}$. While no conclusion about the statistically stored dislocations can be drawn from the analysis of the PED patterns, it is clear that the dislocation structures are not PSB-like dipole configurations. Hence, the corresponding density of statistically stored dislocations can be expected to be much lower than the GND density. This is in very good agreement with dislocation densities typically reported for veins, e.g., $\approx 10^{15}\mathrm{m}^{-2}$ reported for dislocation veins in copper [34].

4. Discussion

4.1. Influence of the grain boundary on dislocation structure formation

If the available volume in a grain is smaller than the dislocation cell size (which is a function of, i.a., applied stress and density, e.g., Ref. [35]), no dislocation patterns or cells will form. For pattern formation to occur, the dislocations need to move and interact with other glissile dislocations, dislocations locks and junctions in order to locally increase the density up to a critical saturation value, at which metastable dislocation structures form [36]. In addition, a grain boundary can affect dislocations through image forces resulting from the elastic anisotropy between two adjacent grains. The image forces may alter the local stress state and enhance the transmission or absorption of dislocations [29]. Generally, image forces arising from free surfaces are assumed to be attractive, while image forces from grain boundaries in most cubic metals are often repulsive [37]. However, results for grain boundaries available from the literature are sparse and almost always obtained for idealized situations of pure edge or pure screw dislocations. In order to estimate the magnitude and direction of image forces acting near the grain boundary in our particular G12 micropillar, a simulation with a

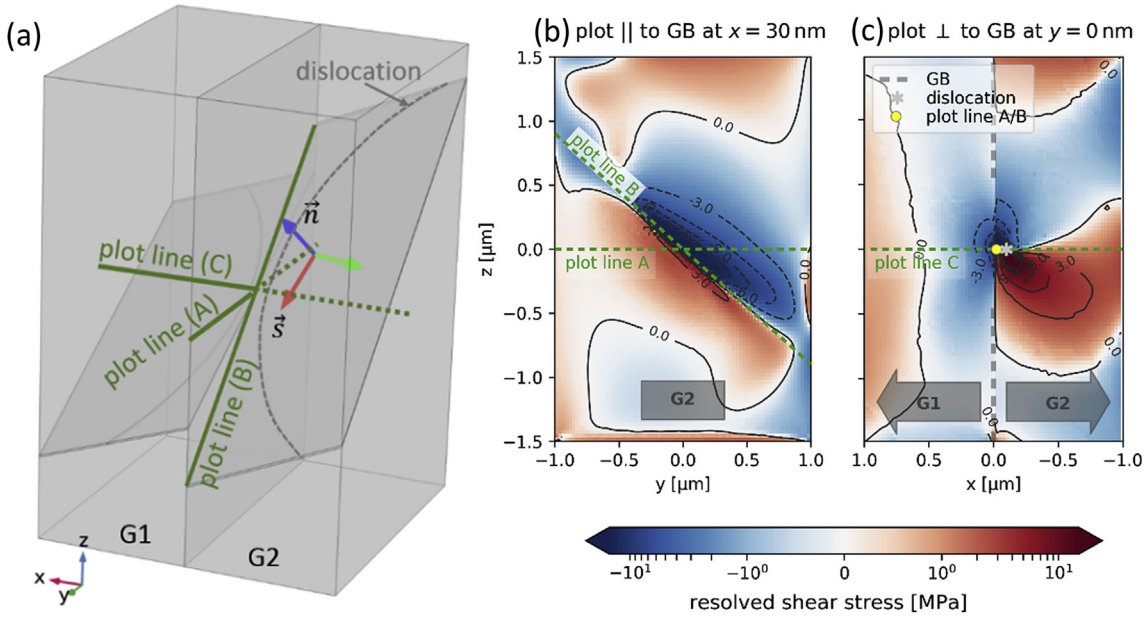

Fig. 9. (a) Geometry of the bicrystal used for the discrete dislocation simulation. The origin of the x-y-z coordinate system is in the center of the pillar, $\vec{n}$ is the slip plane normal and $\vec{s}$ the slip direction parallel to the Burgers vector $\vec{b}$. (b) and (c) show the RSS for the $(111)[01\bar{1}]$ G2 system near the grain boundary plane (left plot) and in a plane cutting perpendicularly through the grain boundary (right plot).

curved dislocation near the grain boundary was performed.

The bicrystal was idealized as depicted in Fig. 9a. For grains G1 and G2, the anisotropic elastic response is given by the three elastic coefficients of the cubic Ni crystal, $C_{11} = 247$ GPa, $C_{44} = 125$ GPa, and $C_{12} = 147$ GPa. The crystal orientations were taken from Table 1. The pillar has a square cross-section of $4\,\mu m^2$, and the grain boundary is a perfect plane dividing the pillar into two grains of equal dimensions that are assumed to be welded perfectly together.

The simulation itself is based on a finite element (FE) approach with element sizes down to a Burgers vector length, $\vec{b}$. A dislocation line is the termination of a plastically swept area, with the surfaces below and above this area displaced by $1\vec{b}$. A very thin layer of height $\Delta h \approx 5 \vee \vec{b} \vee$, within which a constant shear eigenstrain $\varepsilon^0 = \left|\vec{b}\right|/\Delta h$ is prescribed, approximates this area. The size of the finite elements is adaptively chosen such that the stress field of a single dislocation can be recovered at all points that are located outside the dislocation core. For further details of this approach see Refs. [21,22]. Since the experiments showed that plastic deformation is initiated in sample G2 instead of G1 (Fig. 3a), the G2 slip-plane $(111)[01\bar{1}]$, which has the higher Schmid factor, was chosen. The curved dislocation on this plane (shown as the dashed gray line in the right half of the pillar in Fig. 9a) has approximately a screw character closest to the grain boundary. At this position, the distance to the grain boundary is ≈ 90 nm. Assuming linear elasticity – no dislocation core effects or atomic details of the grain boundary are considered – the stresses resulting from multiple dislocations can be additively superimposed and, thus, for simplicity, only a single dislocation is considered in this study. The pillar is fixed at the bottom; no external tractions or displacements are prescribed.

The resulting RSSs for the bicrystal are shown in Fig. 9b and c. The narrow red area at the bottom of the plot in Fig. 9b (corresponding to the center of the plot in Fig. 9c) results from the elastic anisotropy and from fixing the pillar at the bottom. The larger red area at the top originates from the interaction of the dislocation with the free surface, resulting in rather high stresses, comparable to those in the vicinity of the dislocation. Stresses above and below the slip plane exhibit a sign change, which is due to the shear stress field of the screw dislocation. Its characteristic shape (the horizontal "8") can to some extent be seen in Fig. 9c. RSSs in the left half of this plot are shown with respect to the slip system of G1. The different crystallographic orientations G1 vs. G2 constitute the reason for the abrupt change of the magnitude of the stress components across the grain boundary and the strong reduction in the G1-half of the pillar. The different crystallographic orientation has an influence on both the elastic properties as well as on the orientation of the G1 slip system (again $(111)[01\bar{1}]$). These two effects together explain why the sample G1 showed reduced dislocation activity in the experiments.

Four simulations representative for different grain configurations were performed to further analyze the interaction between dislocations and the grain boundary. In all cases, the dislocation remains fixed at its initial position and only the stresses resulting from this stationary situation were computed and analyzed. The four configurations are the following:

As before, true crystallographic orientations according to the experimental data were used for G1 and G2, effectively representing a G12 bicrystal (Fig. 9b), shown as solid black lines in Fig. 10 for the corresponding stresses;

i. the G2 crystal orientation was also used for the G1 part, effectively yielding a larger G2 single crystal without grain boundary (dash-dotted green line in Fig. 10);
ii. the G1 part of the pillar was removed yielding the G2 orientation only, resulting in a free surface instead of the grain boundary (dashed red line in Fig. 10);
iii. for G1, a very stiff material is assumed (Young's modulus $E_{G1} \approx 100E_{G2}$) resulting in a perfectly blocking, very stiff grain boundary (dotted blue line in Fig. 10)).

Comparing the RSS inside G2 for (i) and (ii) in the vicinity of the grain boundary (Fig. 10a and b), it can be seen that the presence of the G1 crystal slightly reduces the local RSS. This difference is due to dislocation image forces resulting from the different elastically anisotropic response of G1 and G2. An estimate for the upper limit of this influence is obtained by the simulation setup (iv) with a perfectly blocking interface. Dislocation stresses are significantly amplified by a factor of ~2.5 compared to the bicrystal. The fundamental characteristics of the stresses, though, remain unaffected inside G2.

For the case of a free surface (lines labeled (iii) in Fig. 10), the

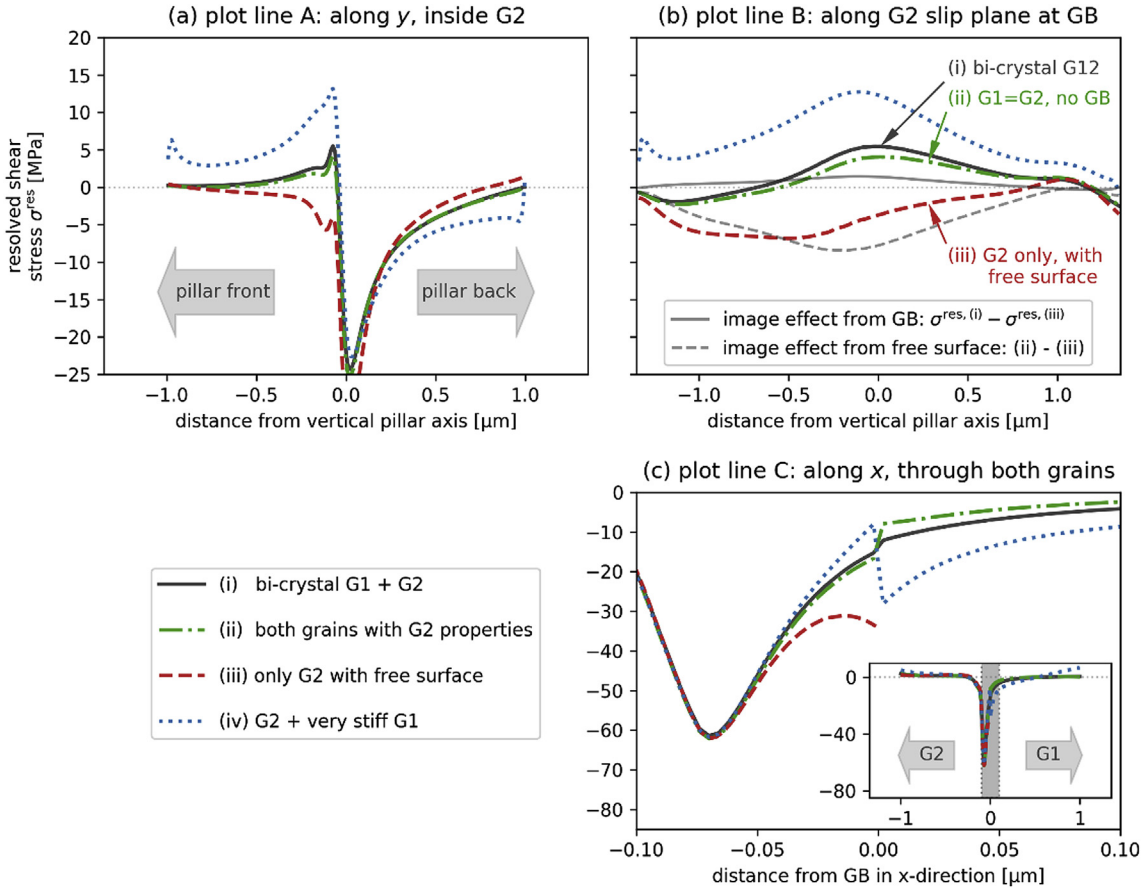

Fig. 10. RSS along three different lines (cf. plot lines in Fig. 9): (a) along a horizontal line parallel to the grain boundary (GB), (b) at a distance of 50 nm of the intersecting line of the G2 slip plane and the GB, and (c) through G1 and G2. The gray box in the inset shows the location of the magnified region around the GB in (c).

stresses are significantly reduced (cf. the red line in Fig. 10b) compared to (i). The difference between the G1 "bulk" simulation (ii) and the "free surface" simulation (iii) (Fig. 10b, gray solid line) is a measure for the strength and direction of the image forces. The fact that the stress level is negative implies that, for the considered (111)[01$\bar{1}$] system, a screw dislocation with line orientation ξ opposite to the Burgers vector direction $\vec{b}/b$ would experience a Peach-Koehler force pointing into negative Burgers vector direction (cf. local coordinate system in Fig. 9). Therefore, the dislocation would experience an attractive force towards the free surface. The grain boundary, however, has the opposite effect. Again, using the "bulk" system (ii) as reference, it is found that the grain boundary exerts a slightly positive stress and, thus, would repel a dislocation (Fig. 10b, gray solid line). This is consistent with calculations presented in Ref. [37], which, though, were conducted for a perfect dislocation only and grain boundaries with three specific misorientation angles.

The effect of the different crystallographic orientations of the G1 and G2 slip systems can be seen in Fig. 10c showing the RSS along a horizontal line cutting through both grains. The influence of the change of slip plane orientation across the grain boundary results in a jump in the stresses, which is less pronounced for the G12 bicrystal than for the "bulk" crystal from simulation (ii) (note that for (ii) only the elastic properties were varied, while keeping the G1 slip system geometry). The reduction of the amplitude of the jump is again the result of the image forces. Moving the dislocation closer to the grain boundary does not change this behavior significantly; only a small shift of the curve (iv) towards the interior of G2 is observed.

From the simulations, we draw the following conclusions: (1) The small magnitude of stresses from image force explain why the dislocation structure of G2 in Fig. 5 is neither strongly attracted nor repelled by the grain boundary. This image effect, however, would become more pronounced when the difference in elastic properties between the two grains were larger. (2) Stresses from dislocation pile-ups in G2 at the grain boundary create only mild stress concentrations on the G1 side (Fig. 9c). This suggests that nucleation events in G1 due to pile-up stress concentrations are relatively unlikely, which is confirmed by our experimental observations. (3) Dislocation structures in G1 seem to accumulate towards the center region of G1 (i.e. forming rather horizontal structures in Fig. 5). This behavior might be related to the stress field shown in Fig. 9c; initially, dislocations are nucleated in G2, and the resulting stress field is a superposition of their individual fields. Since the exact dislocation position in G2 plays a minor role for the stresses in G1, the resulting stress field will look qualitatively similar to that in Fig. 9c. The G1 grain exhibits vertical bands of positive (left = close to the free surface), zero (center of G1), and negative stresses (close to the grain boundary), such that in G1 a newly nucleated dislocation would always move to the center where the stress is zero.

5. Conclusions

Dislocation patterns were observed in the microstructure of Ni single crystal micropillars subjected to cyclic compression loading. ACOM-TEM and Nanostrain mapping techniques revealed the local lattice rotations at the position of the dislocation walls and the associated local strain fields. The excess dislocation density in the dense dislocation wall-structures, the predominant dislocation character as well as the Burgers vector orientation were determined by combining the experimental observation and computational analysis. The main finding of the work is that the grain boundary hinder the formation of

dislocation patterns in the microstructure of a cyclically deformed micropillar. The image forces associated with the grain boundary in this specific bicrystal configuration have only a minor influence on internal stresses in the grain boundary region. The bicrystal behaves– from the point of view of image forces– almost identical to a bulk system. Thus, grain boundary image forces can be excluded as a reason for the reduced occurrence of "mature" cell walls in the bicrystal. Therefore, it is suggested that the reason is indeed the available volume, which is simply too small to accommodate cell structures that would form under the given conditions of stress and dislocation density [38]. Higher load or plastic strain amplitudes might result in dislocation patterns with different characteristic length scales.

Declarations of interest

None.

Contributions

J.G. conducted the in-situ SEM experiments. V.S. and H.I. performed the post mortem TEM investigations. S.S. designed and performed the simulations. V.S., S.S., and R.S. wrote the manuscript. D.S., H.I., S.S. and R.S. designed the study. All authors participated in the discussion and interpretation of the results.

Data availability

The raw/processed data required to reproduce these findings can be found in the corresponding *Data in Brief* article.

Acknowledgments

Financial support from the Flemish (FWO) and German Research Foundation (DFG) through the European M-ERA.NET project "FaSS" (Fatigue Simulation near Surfaces) under the grant numbers GA.014.13 N,SCHW855/5-1, and SA2292/2-1 is gratefully acknowledged. V.S. acknowledges the FWO research project G012012 N "Understanding nanocrystalline mechanical behaviour from structural investigations". H.I. is mandated by the Belgian National Fund for Scientific Research (FSR-FNRS). S.S. acknowledges financial support from the European Research Council through the ERC Grant Agreement No. 759419 (MuDiLingo – A Multiscale Dislocation Language for Data- Driven Materials Science).

References

[1] M.D. Uchic, P.A. Shade, D.M. Dimiduk, Micro-compression testing of fcc metals: a selected overview of experiments and simulations, JOM 61 (3) (2009) 36–41.
[2] M.D. Uchic, P.A. Shade, D.M. Dimiduk, Plasticity of micrometer-scale single crystals in compression, Annu. Rev. Mater. Res. 39 (1) (2009) 361–386.
[3] J.R. Greer, W.D. Nix, Nanoscale gold pillars strengthened through dislocation starvation, Phys. Rev. B73 (245410) (2006) 6.
[4] Z.W. Shan, R.K. Mishra, S.A. Syed Asif, O.L. Warren, A.M. Minor, Mechanical annealing and source-limited deformation in submicrometre-diameter Ni crystals, Nat. Mater. 7 (2) (2008) 115–119.
[5] V.S. Deshpande, A. Needleman, E. Van der Giessen, Plasticity size effects in tension and compression of single crystals, J. Mech. Phys. Solids 53 (12) (2005) 2661–2691.
[6] S.I. Rao, D.M. Dimiduk, M. Tang, M.D. Uchic, T.A. Parthasarathy, C. Woodward, Estimating the strength of single-ended dislocation sources in micron-sized single crystals, Philos. Mag. 87 (30) (2007) 4777–4794.
[7] H. Tang, K.W. Schwarz, H.D. Espinosa, Dislocation escape-related size effects in single-crystal micropillars under uniaxial compression, Acta Mater. 55 (5) (2007) 1607–1616.
[8] S.H. Oh, M. Legros, D. Kiener, G. Dehm, In situ observation of dislocation nucleation and escape in a submicrometre aluminium single crystal, Nat. Mater. 8 (2009) 95.
[9] D.M. Norfleet, D.M. Dimiduk, S.J. Polasik, M.D. Uchic, M.J. Mills, Dislocation structures and their relationship to strength in deformed nickel microcrystals, Acta Mater. 56 (13) (2008) 2988–3001.
[10] C.P. Frick, B.G. Clark, S. Orso, A.S. Schneider, E. Arzt, Size effect on strength and strain hardening of small-scale [111] nickel compression pillars, Mater. Sci. Eng. A 489 (1) (2008) 319–329.
[11] Z.J. Wang, Q.J. Li, Y.N. Cui, Z.L. Liu, E. Ma, J. Li, J. Sun, Z. Zhuang, M. Dao, Z.W. Shan, S. Suresh, Cyclic deformation leads to defect healing and strengthening of small-volume metal crystals, Proc. Natl. Acad. Sci. U.S.A. 112 (44) (2015) 13502–13507.
[12] S. Suresh, Fatique of Materials, Cambridge University Press, 2004.
[13] R. Schwaiger, G. Dehm, O. Kraft, Cyclic deformation of polycrystalline Cu films, Philos. Mag. 83 (6) (2003) 693–710.
[14] G.P. Zhang, R. Schwaiger, C.A. Volkert, O. Kraft, Effect of film thickness and grain size on fatigue-induced dislocation structures in Cu thin films, Philos. Mag. Lett. 83 (8) (2003) 477–483.
[15] M. Sangid, T. Ezaz, H. Sehitoglu, I. Robertson, Energy of slip transmission and nucleation at grain boundaries, Acta Mater. 59 (2011) 283–296.
[16] P.J. Imrich, C. Kirchlechner, C. Motz, G. Dehm, Differences in deformation behavior of bicrystalline Cu micropillars containing a twin boundary or a large-angle grain boundary, Acta Mater. 73 (0) (2014) 240–250.
[17] K.S. Ng, A.H.W. Ngan, Deformation of micron-sized aluminium bi-crystal pillars, Philos. Mag. 89 (33) (2009) 3013–3026.
[18] N. Kheradmand, H. Vehoff, A. Barnoush, An insight into the role of the grain boundary in plastic deformation by means of a bicrystalline pillar compression test and atomistic simulation, Acta Mater. 61 (19) (2013) 7454–7465.
[19] N. Kheradmand, H. Vehoff, Orientation gradients at boundaries in micron-sized bicrystals, Adv. Eng. Mater. 14 (3) (2012) 153–161.
[20] N.V. Malyar, J.S. Micha, G. Dehm, C. Kirchlechner, Dislocation-twin boundary interaction in small scale Cu bi-crystals loaded in different crystallographic directions, Acta Mater. 129 (2017) 91–97.
[21] S. Sandfeld, M. Monavari, M. Zaiser, From systems of discrete dislocations to a continuous field description: stresses and averaging aspects, Model. Simul. Mater. Sci. Eng. 21 (8) (2013) 085006.
[22] O. Jamond, R. Gatti, A. Roos, B. Devincre, Consistent formulation for the Discrete-Continuous Model: improving complex dislocation dynamics simulations, Int. J. Plast. 80 (2016) 19–37.
[23] A.M. Hussein, J.A. El-Awady, Quantifying dislocation microstructure evolution and cyclic hardening in fatigued face-centered cubic single crystals, J. Mech. Phys. Solids 91 (2016) 126–144.
[24] B. Merle, H.W. Höppel, Microscale high-cycle fatigue testing by dynamic micropillar compression using continuous stiffness measurement, Exp. Mech. 58 (3) (2018) 465–474.
[25] R. Schwaiger, M. Weber, B. Moser, P. Gumbsch, O. Kraft, Mechanical assessment of ultrafine-grained nickel by microcompression experiment and finite element simulation, J. Mater. Res. 27 (1) (2012) 266–277.
[26] D. Kiener, C. Motz, G. Dehm, Dislocation-induced crystal rotations in micro-compressed single crystal copper columns, J. Mater. Sci. 43 (7) (2008) 2503–2506.
[27] C. Kirchlechner, J. Keckes, C. Motz, W. Grosinger, M.W. Kapp, J.S. Micha, O. Ulrich, G. Dehm, Impact of instrumental constraints and imperfections on the dislocation structure in micron-sized Cu compression pillars, Acta Mater. 59 (14) (2011) 5618–5626.
[28] P. Li, S.X. Li, Z.G. Wang, Z.F. Zhang, Fundamental factors on formation mechanism of dislocation arrangements in cyclically deformed fcc single crystals, Prog. Mater. Sci. 56 (3) (2011) 328–377.
[29] Q. Yu, R.K. Mishra, J.W. Morris, A.M. Minor, The effect of size on dislocation cell formation and strain hardening in aluminium, Philos. Mag. 94 (18) (2014) 2062–2071.
[30] M.P. Vigouroux, V. Delaye, N. Bernier, R. Cipro, D. Lafond, G. Audoit, T. Baron, J.L. Rouvière, M. Martin, B. Chenevier, F. Bertin, Strain mapping at the nanoscale using precession electron diffraction in transmission electron microscope with off axis camera, Appl. Phys. Lett. 105 (19) (2014) 191906.
[31] E.F. Rauch, M. Véron, Automated crystal orientation and phase mapping in TEM, Mater. Char. 98 (0) (2014) 1–9.
[32] S.I. Rao, D.M. Dimiduk, J.A. El-Awady, T.A. Parthasarathy, M.D. Uchic, C. Woodward, Atomistic simulations of cross-slip nucleation at screw dislocation intersections in face-centered cubic nickel, Philos. Mag. 89 (34–36) (2009) 3351–3369.
[33] A.M. Hussein, S.I. Rao, M.D. Uchic, D.M. Dimiduk, J.A. El-Awady, Microstructurally based cross-slip mechanisms and their effects on dislocation microstructure evolution in fcc crystals, Acta Mater. 85 (0) (2015) 180–190.
[34] H. Mughbrabi, F.U. Ackermann, K. Herz, J.T. Fong (Ed.), Persistent slipbands in fatigued face-centered and body-centered cubic metals, ASTM International, West Conshohocken, PA, 1979, pp. 69–105.
[35] M. Sauzay, L.P. Kubin, Scaling laws for dislocation microstructures in monotonic and cyclic deformation of fcc metals, Prog. Mater. Sci. 56 (2011) 725–784.
[36] S. Sandfeld, M. Zaiser, Pattern formation in a minimal model of continuum dislocation plasticity, Model. Simul. Mater. Sci. Eng. 23 (6) (2015) 065005.
[37] L. Priester, Grain Boundaries from Theory to Engineering, springer, 2013.
[38] M. Zaiser, S. Sandfeld, Scaling properties of dislocation simulations in the similitude regime, Model. Simul. Mater. Sci. Eng. 22 (6) (2014) 065012.